

Design of perfectly conducting objects that are invisible to an incident plane wave*

Johan Helsing[†] Shidong Jiang[‡] Anders Karlsson[§]

(March 4, 2024)

Abstract

This work concerns the design of perfectly conducting objects that are invisible to an incident transverse magnetic plane wave. The object in question is a finite planar waveguide with a finite periodic array of barriers. By optimizing this array, the amplitude of the scattered field is reduced to less than 10^{-9} times the amplitude of the incident plane wave everywhere outside the waveguide. To accurately evaluate such minute amplitudes, we employ a recently developed boundary integral equation technique, adapted for objects whose boundaries have endpoints, corners, and branch points.

1 Introduction

This work is about the design of perfectly electrically conducting (PEC) objects that, in a narrow frequency band, become almost invisible to an incident plane wave in free space. The objects consist of a finite planar waveguide, that is, two parallel PEC plates, loaded with a finite periodic array of PEC barriers. Such barrier-loaded (B-L) waveguides may serve as spatial band pass filters and they can make other objects invisible by hiding them in their interiors. The boundaries of the B-L waveguides have sharp corners, branch points and endpoints and these *singular boundary points* create challenges for numerical solvers regardless of what numerical method they are based on. We have the ambitious criteria for invisibility that, at the center frequency, the amplitude of the scattered field is less than 10^{-9} times the amplitude of the incident field everywhere outside the waveguide.

*This work was supported by the Swedish Research Council under contract 2021-03720.

[†]Centre for Mathematical Sciences, Lund University Box 118, 221 00 Lund, Sweden (johan.helsing@math.lth.se)

[‡]Center for Computational Mathematics, Flatiron Institute, Simons Foundation, New York, New York 10010 (sjiang@flatironinstitute.org)

[§]Electrical and Information Technology, Lund University, Box 118, 221 00 Lund, Sweden (anders.karlsson@eit.lth.se)

This is to prove that the B-L waveguides can be used as high quality spatial band pass filters. The most common boundary integral equation (BIE) techniques, the finite element method (FEM), and finite difference time domain techniques do not offer the accuracy we require for geometries with singular boundary points. For this reason we use a recently developed BIE technique adapted for singular geometries.

A historical review of the design of invisible objects, both in science and fiction, is given in [12]. The research received a boost in 2006, when articles on cloaking began to appear. Cloaking means that an object is made invisible by covering it with a coating that causes an incident wave to travel around the object such that no scattered wave is produced. The search for materials suitable for cloaking in turn led to intensive research in the field of metamaterials. These materials are man-made and are designed to possess properties not found in nature, as seen in the reviews [11, 20]. Despite progress in the field of metamaterials, a major breakthrough of cloaking technology still lies in the future.

Another type of objects that can be made invisible are the so called frequency selective structures (FSS) [3, 21]. They often consist of single- or multi-layer elements periodically arranged in a plane, and can be designed to be invisible in a certain frequency band and highly reflecting at other frequencies. The FSS are particularly important in radar applications, but they also occur in other applications such as dichroic sub-reflectors, microwave lenses, and electromagnetic interference protection.

In the frequency band where the B-L waveguide is invisible, the wave transmitted through the array of barriers has the same amplitude as the incident plane wave. This is also the case for the transmitted wave in certain types of microwave band-pass filters [6] and infinite or semi-infinite waveguides designed to make objects invisible [5, 8]. In contrast to the waveguides in [5] and [6], the transmitted wave of a B-L waveguide must equal the incident wave. This condition complicates the design of the B-L waveguide. In [8], an object inside a waveguide is made invisible by deforming the walls of the waveguide. It is an interesting approach, but it cannot be applied here because the walls of the B-L waveguides must be planar.

Cloaked objects, FSS, and B-L waveguides can only be invisible in a narrow frequency band. This is crucial for the B-L waveguides and for the FSS, because frequency filtering is an important application, but it is an undesirable feature for cloaked objects. Despite geometric differences between the FSS and the B-L waveguides, there are phenomenological similarities, suggesting that B-L waveguides can be an alternative to FSS in certain applications. The B-L waveguides are only infinite along one spatial direction, whereas the FSS are infinite along two directions. Thus several B-L waveguides can be combined to form large invisible structures, which, for instance, is a desirable feature when designing radomes for radar. On the other hand, the FSS can be made much thinner than one wavelength, while the B-L

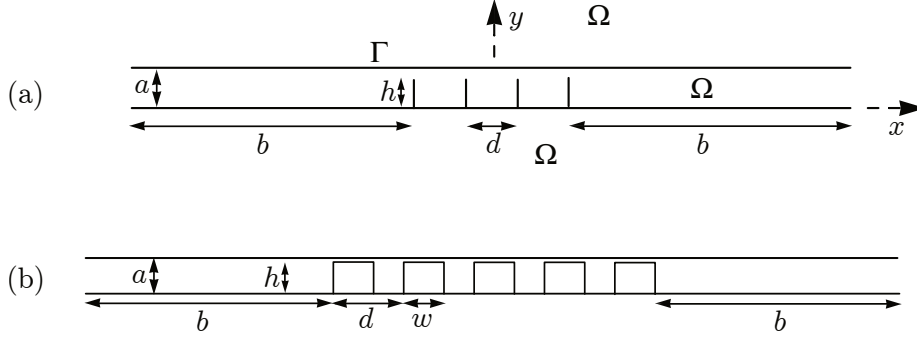


Figure 1: The 2D geometric cross section of two waveguides, translationally invariant in the z -direction; (a) B-L waveguide with four infinitely thin strips. The strips are attached to the lower wall. Γ is the union of the upper and lower walls, both of length $2b + 3d$, and the strips with total length $4h$. Ω is the domain outside Γ in the xy -plane; (b) B-L waveguide with five rectangular bars. The bars are attached to the lower wall.

waveguides are at least half a wavelength wide.

The paper is organized as follows. Section 2 formulates the scattering problem and presents two types of B-L waveguides. Section 3 is about our BIE-based numerical scheme for PEC objects with singular boundary points. Several designs of B-L waveguides that are invisible in prescribed frequency bands are presented in Section 4. Section 5 contains conclusions.

2 Problem formulation

We consider a time harmonic in-plane transverse magnetic (TM) wave impinging on an object consisting of two disjoint PEC parts of infinite extension in the z -direction, but bounded in the xy -plane. The time dependence is $e^{-i\omega t}$ and $r = (x, y)$. The total magnetic field is $\mathbf{H}(r) = u(r)\hat{z}$ with decomposition

$$u(r) = u^{\text{in}}(x) + u^{\text{sc}}(r), \quad (1)$$

where $u^{\text{in}}(x) = e^{ikx}$ is the incident field and $u^{\text{sc}}(r)$ is the scattered field. Since the waveguide is translationally invariant in the z -direction, the 3D Maxwell's equations are reduced to a scalar 2D problem in the xy -plane.

The boundary in the xy -plane is Γ . We provide Γ with an orientation so that an outward unit normal $\nu = (\nu_x, \nu_y)$ can be defined. The domain outside Γ , in the xy -plane, is denoted Ω . In Ω there is air ($\varepsilon_r = 1$) and the wavenumber is k . The side of Γ from which ν is directed is the positive side and the other side is the negative side.

The scattering problem under study can be formulated as a boundary

value problem (BVP) for the Helmholtz equation

$$\nabla^2 u(r) + k^2 u(r) = 0, \quad r \in \Omega, \quad (2)$$

$$\nu \cdot \nabla u(r) = 0, \quad r \in \Gamma, \quad (3)$$

$$u(r) = e^{ikx} + u^{\text{sc}}(r), \quad r \in \Omega, \quad (4)$$

$$u^{\text{sc}}(r) = \frac{e^{ik|r|}}{\sqrt{|r|}} (F(r/|r|) + \mathcal{O}(|r|^{-1})), \quad |r| \rightarrow \infty, \quad (5)$$

where (3) is the PEC boundary condition and $F(r/|r|)$ is the far-field amplitude.

The fundamental solution to Helmholtz equation in the plane is

$$\Phi_k(r, r') = \frac{i}{4} H_0^{(1)}(k|r - r'|), \quad (6)$$

where $H_0^{(1)}$ is the zeroth-order Hankel function of the first kind. The standard integral representation of $u^{\text{sc}}(r)$ follows from Green's theorem [4, p. 61] and reads

$$u^{\text{sc}}(r) = \int_{\Gamma} v(r') \frac{\partial \Phi_k(r, r')}{\partial \nu'} d\ell', \quad (7)$$

where $d\ell'$ is an element of arc length and $\partial/\partial \nu' = \nu(r') \cdot \nabla'$. The function $v(r')$ is given by

$$v(r') = \begin{cases} u^{\text{sc}}(r'), & \text{on closed parts of } \Gamma, \\ u^{\text{sc}+}(r') - u^{\text{sc}-}(r'), & \text{on open parts of } \Gamma, \end{cases} \quad (8)$$

where $u^{\text{sc}+}(r)$ is the scattered field on the positive side of Γ and $u^{\text{sc}-}(r)$ on the negative side.

The invisible planar B-L waveguides designed in this work are shown in Figure 1 and they are invisible only in a single frequency band. Their walls should be as thin as possible, and it is reasonable to model them with zero thickness. The B-L waveguides then have endpoints and branch points, regardless of the shape of the barriers.

The strips in Figure 1(a) have zero thickness and height $h < a$. The rectangular barriers in Figure 1(b) have height $h < a$ and width w . The boundary of each rectangular barrier is, thus, a closed part of Γ .

A B-L waveguide is defined to be invisible at a wavenumber k if, at that k , $|u^{\text{sc}}(r)| < 10^{-9}$ outside the waveguide. That is, outside the smallest rectangular domain that encloses the waveguide. The B-L waveguides have unit inter-wall distance and are designed to be invisible at k via optimization. In the optimization process we also require that the scattering cross section σ^{sc} , a scalar quantity defined in (9) below, is less than $2\pi \cdot 10^{-18}$. This bound on σ^{sc} can be shown to hold if the bound on $|u^{\text{sc}}(r)|$ holds. As a comparison,

a metal wire of unit radius has a radar cross section of four length units in the high frequency limit.

The procedure for designing the invisible waveguides in Figure 1 is to first let $a = 1$, then choose fix values of b , h , and w , and finally use optimization to find k and d such that $\sigma^{\text{sc}} < 2\pi \cdot 10^{-18}$. Once k and d are determined, we check that $|u^{\text{sc}}(r)| < 10^{-9}$ outside the waveguide. It should be noted that one can change k to a desired value by scaling the geometry. Below, in Section 2.2, we derive an approximate relation that k and d must satisfy in order for the waveguides to be invisible. This relation is used to find initial guesses for k and d .

The scattering cross section is defined as

$$\sigma^{\text{sc}} \equiv \frac{\text{time average of scattered power}}{\text{time average of incident power density}}. \quad (9)$$

There are several mathematically equivalent expressions for σ^{sc} . Our preferred choice for numerical evaluation in this work is

$$\sigma^{\text{sc}} = \frac{1}{k} \text{Im} \left\{ \int_0^{2\pi} \frac{\partial u^{\text{sc}}(r')}{\partial |r'|} u^{\text{sc}*}(r') |r'| d\phi' \right\}, \quad (10)$$

which follows from (9) and Poynting's theorem. Here $r' = |r'|(\cos \phi', \sin \phi')$ is a point on a circle that circumscribes the geometric cross section of the object and the asterisk denotes the complex conjugate.

2.1 Waveguide modes

To illustrate the physics of the B-L waveguides one can use the concept of waveguide *modes*. Waveguide theory says that in all sections of the waveguide where there are no barriers, the total field is a sum of waveguide modes such that

$$u(r) = \sum_{p=0}^{\infty} (\alpha_p e^{ik_p x} + \beta_p e^{-ik_p x}) \cos(p\pi y/a), \quad (11)$$

where the wavenumber k_p is given by

$$k_p = \sqrt{k^2 - (p\pi/a)^2}, \quad (12)$$

and where the amplitudes α_p and β_p have different values in all waveguide sections. The transverse electromagnetic (TEM) mode has $p = 0$. Higher-order modes have $p > 0$. At the entrance of the waveguides in Figure 1 the incident TM wave couples to the TEM mode and the higher-order modes.

A waveguide structure is invisible if the reflected TEM mode is zero at the entrance and the transmitted TEM mode equals the incident wave at the exit. To achieve this, the condition $k < \pi/a$ is used, which means that all higher-order modes are evanescent. Furthermore, these modes must decay fast enough for their amplitudes to be negligible at the entrance and exit of the waveguide.

2.2 A relation between the wavenumber k and the period d

From the integral representation (7) it follows that the scattered far field in the forward and backward directions are

$$\lim_{x \rightarrow \pm\infty} u^{\text{sc}}(x, 0) = \pm \sqrt{\frac{k}{8\pi|x|}} e^{i(k|x| - \pi/4)} \int_{\Gamma} \nu'_x v(r') e^{\mp i k x'} d\ell'. \quad (13)$$

As ν'_x is zero on the horizontal walls, only the barriers contribute to the integral. When there is no reflected TEM mode to the left of the first barrier there exists a wavenumber k_s for which $\nu'_x v(r') e^{-i k_s x'}$ is almost the same on all barriers. This is so because the barriers form a finite periodic array, and it is confirmed in our numerical experiments. Thus, from (13),

$$\lim_{x \rightarrow \pm\infty} u^{\text{sc}}(x, 0) \sim \frac{1}{\sqrt{|x|}} \frac{1 - e^{i(k_s \mp k)n_{\text{bar}}d}}{1 - e^{i(k_s \mp k)d}}, \quad (14)$$

where n_{bar} is the number of barriers.

The two-dimensional optical theorem [17, eq. (39)]

$$\sigma^{\text{sc}} = - \lim_{x \rightarrow \infty} \sqrt{\frac{8\pi x}{k}} \text{Re} \left\{ u^{\text{sc}}(x, 0) e^{-i(kx - \pi/4)} \right\} \quad (15)$$

states that a necessary and sufficient condition for $\sigma^{\text{sc}} = 0$ is $\lim_{x \rightarrow \infty} \sqrt{x} u^{\text{sc}}(x, 0) = 0$. Another necessary condition for invisibility is $\lim_{x \rightarrow -\infty} \sqrt{|x|} u^{\text{sc}}(x, 0) = 0$, as seen from (10). A relation between k and d , and also a relation between k_s and d , now follows by applying $\lim_{x \rightarrow \pm\infty} \sqrt{|x|} u^{\text{sc}}(x, 0) = 0$ to (14):

$$k n_{\text{bar}} d \approx n\pi, \quad (16)$$

$$k_s n_{\text{bar}} d \approx n\pi + 2m\pi, \quad (17)$$

where $n, m > 0$ are integers. Although approximate, (16) holds to at least three digits for the invisible waveguides that we have designed in this work.

3 Numerical scheme

In this section we first derive the BIE reformulation of the BVP (2), (3), (4), and (5), upon which our numerical scheme is based. Then we discuss how to efficiently discretize and solve this BIE in the presence of singular boundary points and how to subsequently evaluate the solution, $u(r)$ or $u^{\text{sc}}(r)$, at points r in the computational domain. We end with some theoretical considerations regarding the second-kindness of our BIE.

3.1 Integral equation reformulation

Let, as in Section 2, Γ be a union of oriented smooth open arcs, referred to collectively as the *boundary*. The outward unit normal at $r \in \Gamma$ is $\nu(r)$. We use standard definitions of the acoustic layer operators S_k , K_k , and T_k [10, pp. 41–42], defined by their action on a layer density $\rho(r)$ on Γ as

$$S_k \rho(r) = 2 \int_{\Gamma} \Phi_k(r, r') \rho(r') d\ell', \quad r \in \Gamma, \quad (18)$$

$$K_k \rho(r) = 2 \int_{\Gamma} \frac{\partial \Phi_k}{\partial \nu'}(r, r') \rho(r') d\ell', \quad r \in \Gamma, \quad (19)$$

$$T_k \rho(r) = 2 \int_{\Gamma} \frac{\partial^2 \Phi_k}{\partial \nu \partial \nu'}(r, r') \rho(r') d\ell', \quad r \in \Gamma, \quad (20)$$

where $\partial/\partial \nu = \nu(r) \cdot \nabla$. For ease of presentation we also use K_k to define the double-layer potential. That is, we use

$$K_k \rho(r) = 2 \int_{\Gamma} \frac{\partial \Phi_k}{\partial \nu'}(r, r') \rho(r') d\ell', \quad r \in \mathbb{R}^2 \setminus \Gamma. \quad (21)$$

Within our BIE framework, the field $u^{\text{sc}}(r)$ of the Neumann Helmholtz problem (2), (3), (4), and (5) has the representation

$$u^{\text{sc}}(r) = K_k(-S_k)\rho(r), \quad r \in \mathbb{R}^2 \setminus \Gamma. \quad (22)$$

This representation is recommended for piecewise smooth open arcs Γ in [16] and also recommended, along with singular weight functions, for everywhere smooth open arcs Γ in [7]. The BIE itself, obtained by inserting (4) with (22) in (3), is

$$T_k(-S_k)\rho(r) = -\nu(r) \cdot \nabla e^{ikx}, \quad r \in \Gamma. \quad (23)$$

We plan to solve (23) for $\rho(r)$ using Nyström discretization accelerated by the recursively compressed inverse preconditioning (RCIP) method. While there is nothing new with using Nyström/RCIP schemes for solving BIEs per se, see [15] and references therein, it may not be obvious which is the best way to apply such schemes to BIEs with composed singular operators as in (23). We therefore now devote Section 3.2 to an overview of this topic.

3.2 Overview of RCIP

The RCIP method accelerates and stabilizes Nyström solvers in certain “singular” situations. More precisely, RCIP applies to the Nyström discretization of Fredholm second kind BIEs on closed or open Γ that contain some type of singular boundary points. Our overview, based on [15, Sections 3 and 16], summarizes the most important features of RCIP with particular emphasis on composed operators. Section 3.2.1 reviews RCIP in a standard setting and Section 3.2.2 shows what modifications are needed for (23). The Nyström discretization is assumed to rely on composite Gauss–Legendre quadrature with 16 nodes per quadrature panel. See [16] for more detail.

3.2.1 A Fredholm integral equation in standard form

We start with a Fredholm second kind BIE on Γ in standard form

$$(I + G) \rho(r) = g(r), \quad r \in \Gamma. \quad (24)$$

Here I is the identity, G is an integral operator that is often assumed compact away from singular boundary points on Γ , $g(r)$ is a piecewise smooth right-hand side, and $\rho(r)$ is the unknown layer density to be solved for.

For simplicity, we only discuss how to deal with one singular point on Γ and denote this point γ . Multiple singular points can be treated independently and in parallel.

Let G be split into two parts

$$G = G^\star + G^\circ, \quad (25)$$

where G^\star describes the kernel interaction close to γ and G° is the (compact) remainder. Let the part of Γ on which G^\star is nonzero be denoted Γ^\star .

Now introduce the *transformed density*

$$\tilde{\rho}(r) = (I + G^\star) \rho(r). \quad (26)$$

Then use (25) and (26) to rewrite (24) as

$$(I + G^\circ(I + G^\star)^{-1}) \tilde{\rho}(r) = g(r), \quad r \in \Gamma. \quad (27)$$

Although (27) looks similar to (24), there are advantages to using (27) rather than (24) from a numerical point of view: the spectral properties of $G^\circ(I + G^\star)^{-1}$ are better than those of G .

The Nyström/RCIP scheme discretizes (27) chiefly on a grid on a *coarse mesh* of panels on Γ that is sufficient to resolve G° and $g(r)$. Only the inverse $(I + G^\star)^{-1}$ needs a grid on a local, dyadically refined, *fine mesh* of panels on Γ^\star . The discretization of (27) takes the form

$$(\mathbf{I}_{\text{coa}} + \mathbf{G}_{\text{coa}}^\circ \mathbf{R}) \tilde{\boldsymbol{\rho}}_{\text{coa}} = \mathbf{g}_{\text{coa}}, \quad (28)$$

where \mathbf{R} is a sparse block matrix called the *compressed inverse* and where the discrete unknown $\tilde{\boldsymbol{\rho}}_{\text{coa}}$ lives on the coarse grid only. The boundary part Γ^\star contains the two, four, or six coarse panels closest to γ depending on if γ is an endpoint, a corner, or a branch point.

The power of RCIP lies in the construction of \mathbf{R} . In theory, \mathbf{R} corresponds to a discretization of $(I + G^\star)^{-1}$ on the fine grid, followed by a lossless compression to the coarse grid. In practice, \mathbf{R} is constructed via a forward recursion on a hierarchy of grids on Γ^\star and where refinement and compression occur in tandem. The computational cost grows, at most, linearly with the number of refinement levels.

Once the compressed equation (28) is solved for $\tilde{\boldsymbol{\rho}}_{\text{coa}}$ and its *weight-corrected* counterpart $\hat{\boldsymbol{\rho}}_{\text{coa}} = \mathbf{R}\tilde{\boldsymbol{\rho}}_{\text{coa}}$ is produced, several useful functionals of $\rho(r)$ can be computed with ease. Should one so wish, the solution $\rho(r)$ on the fine grid can be reconstructed from $\tilde{\boldsymbol{\rho}}_{\text{coa}}$ via a backward recursion on the same hierarchy of grids that is used in the construction of \mathbf{R} .

3.2.2 An integral equation with composed operators

The BIE (23), that needs to be solved in the present work, is cast in the form

$$A(-B)\rho_1(r) = g(r), \quad r \in \Gamma, \quad (29)$$

where the unknown density now is denoted $\rho_1(r)$ and where $A = T_k$, $B = S_k$, and $g(r) = -\nu(r) \cdot \nabla e^{ikx}$. Clearly, the composition of A and $-B$ and the absence of I make (29) look quite different from the standard form (24). It should be noted, however, that for versions of $A = T_k$ and $B = S_k$, weighted as in Chebyshev–Gauss quadrature, and on smooth open Γ , the BIE (29) is mathematically equivalent to a BIE in the form (24) with G being a compact operator [7, Theorem 1].

We now apply the Nyström/RCIP scheme of Section 3.2.1 to (29), with the goal to find the analogue of the compressed discrete equation (28) for (29). First, introduce the new temporary density $\rho_2(r)$ via

$$\rho_2(r) = -B\rho_1(r). \quad (30)$$

This allows us to rewrite (29) as the 2×2 block system

$$\left(\begin{bmatrix} I & 0 \\ 0 & I \end{bmatrix} + \begin{bmatrix} -I & A \\ B & 0 \end{bmatrix} \right) \begin{bmatrix} \rho_1(r) \\ \rho_2(r) \end{bmatrix} = \begin{bmatrix} g(r) \\ 0 \end{bmatrix}, \quad (31)$$

which corresponds to (24) in Section 3.2.1.

Note that (31) is free from composed operators so that the Nyström/RCIP scheme can be applied. The analogue of (27) is

$$\left(\begin{bmatrix} I & 0 \\ 0 & I \end{bmatrix} + \begin{bmatrix} -I^\circ & A^\circ \\ B^\circ & 0 \end{bmatrix} \left(\begin{bmatrix} I & 0 \\ 0 & I \end{bmatrix} + \begin{bmatrix} -I^\star & A^\star \\ B^\star & 0 \end{bmatrix} \right)^{-1} \right) \begin{bmatrix} \tilde{\rho}_1(r) \\ \tilde{\rho}_2(r) \end{bmatrix} = \begin{bmatrix} g(r) \\ 0 \end{bmatrix}. \quad (32)$$

The analogue of (28) is

$$\left(\begin{bmatrix} \mathbf{I}_{\text{coa}} & \mathbf{0}_{\text{coa}} \\ \mathbf{0}_{\text{coa}} & \mathbf{I}_{\text{coa}} \end{bmatrix} + \begin{bmatrix} -\mathbf{I}_{\text{coa}}^\circ & \mathbf{A}_{\text{coa}}^\circ \\ \mathbf{B}_{\text{coa}}^\circ & \mathbf{0}_{\text{coa}} \end{bmatrix} \begin{bmatrix} \mathbf{R}_1 & \mathbf{R}_3 \\ \mathbf{R}_2 & \mathbf{R}_4 \end{bmatrix} \right) \begin{bmatrix} \tilde{\boldsymbol{\rho}}_{1\text{coa}} \\ \tilde{\boldsymbol{\rho}}_{2\text{coa}} \end{bmatrix} = \begin{bmatrix} \mathbf{g}_{\text{coa}} \\ 0 \end{bmatrix}. \quad (33)$$

Here we have partitioned the compressed inverse \mathbf{R} into the four sparse equi-sized blocks \mathbf{R}_1 , \mathbf{R}_2 , \mathbf{R}_3 , and $\mathbf{R}_4 = \mathbf{I}_{\text{coa}}^\circ$.

As an extra twist, we write the compressed equation (33) as a linear system involving only one discrete density – not two. To this end, introduce the new density $\tilde{\rho}_{\text{coa}}$ via

$$\tilde{\rho}_{1\text{coa}} = \tilde{\rho}_{\text{coa}} + \mathbf{R}_1^{-1} \mathbf{R}_3 \mathbf{B}_{\text{coa}}^{\circ} \mathbf{R}_1 \tilde{\rho}_{\text{coa}}, \quad (34)$$

$$\tilde{\rho}_{2\text{coa}} = -\mathbf{B}_{\text{coa}}^{\circ} \mathbf{R}_1 \tilde{\rho}_{\text{coa}}. \quad (35)$$

The change of variables (34) and (35) is chosen so that the second block-row of (33) is automatically satisfied. The first block-row of (33) becomes

$$\begin{aligned} [\mathbf{I}_{\text{coa}}^* - \mathbf{A}_{\text{coa}}^{\circ} (\mathbf{R}_4 - \mathbf{R}_2 \mathbf{R}_1^{-1} \mathbf{R}_3) \mathbf{B}_{\text{coa}}^{\circ} \mathbf{R}_1 + \mathbf{A}_{\text{coa}}^{\circ} \mathbf{R}_2 \\ + \mathbf{R}_1^{-1} \mathbf{R}_3 \mathbf{B}_{\text{coa}}^{\circ} \mathbf{R}_1] \tilde{\rho}_{\text{coa}} = \mathbf{g}_{\text{coa}}. \end{aligned} \quad (36)$$

We observe, from (34), that away from Γ^* the discrete density $\tilde{\rho}_{\text{coa}}$ coincides with $\tilde{\rho}_{1\text{coa}}$. Therefore one can expect the system (36) to share more properties with the original equation (29) than the expanded system (33). Numerical experiments indicate that (36) is superior to (33) not only in terms of computational economy, but also in terms of stability and of convergence of iterative solvers.

3.3 On-surface and near-field evaluation

The discretization of the BIE (29) on Γ involves the discretization of integrals with various types of singular integrands. Furthermore, for r close to Γ , the discretization of the field representation (22) involves various types of nearly singular integrands. These singular and nearly singular integrals can, typically, not be accurately evaluated at a reasonable cost using composite standard interpolatory quadrature, but require special discretization techniques. For this, we use a panel-based product integration scheme which, according to the classification of [14], is “explicit split”.

Our panel-based explicit-split quadrature scheme is described in detail in [18, Section 4]. For now, we only mention that the scheme combines recursion with analytical methods such as the use of the fundamental theorem of complex line integrals. Vectors r and r' in the real plane \mathbb{R}^2 are identified with points z and τ in the complex plane \mathbb{C} . Nearly singular and singular integral operator kernels $G(r, r')$ are split according to the general pattern

$$\begin{aligned} G(r, r') d\ell' = G_0(r, r') d\ell' + \log |r - r'| G_L(r, r') d\ell' \\ + c_C \text{Re} \left\{ \frac{G_C(z, \tau) d\tau}{i(\tau - z)} \right\} + \text{Re} \left\{ \frac{G_H(z, \tau) d\tau}{i(\tau - z)^2} \right\}. \end{aligned} \quad (37)$$

Here c_C is a, possibly complex, constant and $G_0(r, r')$, $G_L(r, r')$, $G_C(z, \tau)$, and $G_H(z, \tau)$ are smooth functions. Our scheme requires explicit formulas for $G(r, r')$, $G_L(r, r')$, $G_C(z, \tau)$, and $G_H(z, \tau)$, while $G_0(r, r')$ needs only to be known in the limit $r' \rightarrow r$. See [2, Section 6.2] for additional remarks.

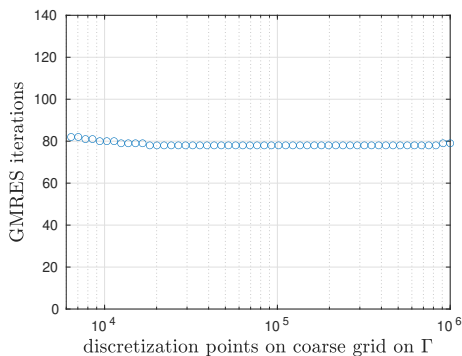


Figure 2: Behavior of (29) with (36) under uniform overresolution for the Neumann Helmholtz problem of scattering of a TM plane wave by the spiral-shaped arc of [7, Figure 2] and with $k = 104.8530264831035$: GMRES iterations for full convergence.

3.4 Second-kindness and compact operators

The assumption, mentioned in Section 3.2.1, that G° of (25) should be compact for RCIP to apply, is actually too restrictive. For example, in [19] it is demonstrated that G° can contain a Cauchy-singular operator: using the GMRES iterative solver in the solve phase, RCIP still works although the number of GMRES iterations needed for convergence may be high due to the presence of multiple accumulation points in the spectrum of G° . See [15, Eq. (24)] for a better, although more technical, assumption about G° .

Allowing G° of (25) to be non-compact is important in the present work. In (29) we view B as a reasonable right preconditioner to A and merely consider $(A(-B) - I)^\circ$ as an operator whose spectrum is clustered.

Some light can be shed on the “second-kindness” of (36) on different Γ by monitoring the convergence of GMRES under uniform overresolution. For example, Figure 2 shows that on a smooth open Γ , the number of GMRES iterations required to meet a small stopping criterion threshold in the relative residual can be bounded – indicating that (36) behaves as a discretization of a BIE in the form (24) with compact G .

A related issue is what the authors of [1] call “numerical second-kindness”: even if a BIE in the form (29) is mathematically equivalent to a second kind BIE (24) with compact $G = A(-B) - I$, it may happen that the GMRES iterations stall. The reason being that $A(-B) - I$ is not available to as high precision as A and B themselves due to numerical cancellation. Then the formulation is said to lack numerical second-kindness [1, Section 6.1]. In the present work we have not observed any such bad behavior.

4 Examples of B-L waveguides

We now present numerical results for two types of B-L waveguides. The numerical codes are written in MATLAB, release 2022a, and executed on a workstation equipped with an Intel Core i7-3930K CPU and 64 GB of RAM. The built-in function `fminsearch` is used for design optimization. The fast multipole method routine `hfmm2d` from [13] is used in connection with matrix-vector multiplication whenever deemed efficient.

When assessing the accuracy of computed fields and scattering cross sections we adopt a procedure where to each numerical solution we also compute an overresolved reference solution, using roughly 50% more points in the discretization of the setup under study and doubled radius $|r'|$ in (10). The absolute difference between the two solutions at a field point is the *estimated absolute pointwise error*. The fields and their errors are always computed at 10^6 field points on a rectangular Cartesian grid in the computational domains shown.

4.1 B-L waveguide with strip barriers

Consider first the design of a B-L waveguide with vertical strips, as in Figure 1(a). The distance between the walls, a , is unity in a suitable unit of length, as stated in Section 2. For waveguides with more than three strips, there is a range for each of b , d , h , and k in which one can find values that give $\sigma^{\text{sc}} < 2\pi \cdot 10^{-18}$. In the examples shown here, values of b and h are first chosen in these ranges. The values of k and d are then determined by `fminsearch` via minimization of σ^{sc} .

Figures 3, 4, 5, and 7 show fields and error estimates computed at field points in the computational domain $\{-40 \leq x \leq 40, -2/3 \leq y \leq 5/3\}$. The x - and y -axes are scaled differently to provide better field resolution inside the waveguide, given the aspect ratio of the images and the range of x . The radius in (10) is chosen as $|r'| = 30$.

4.1.1 B-L waveguide with four strips

The first example is a four-strip waveguide with $a = 1$, $b = 7.3$ and $h = 0.9973$. Optimization gives $\sigma^{\text{sc}} \approx 2 \cdot 10^{-21}$ at $k = 0.5712887729818$ and $d = 1.373106370502$. This σ^{sc} is small enough to be at the overall noise level of the numerical scheme. Figure 3(a) shows the waveguide. The gaps between the endpoints of the strips and the upper wall are too small to be seen. Figure 3(b) shows the real part of $u(r)$. Only in the regions between the strips is there a noticeable difference between $u(r)$ and $u^{\text{in}}(x)$. The field pattern shows that $n = 1$ and $m = 1$ in (16) and (17). The \log_{10} of $|u^{\text{sc}}(r)|$ is shown in Figure 3(c). From the first strip to the waveguide entrance, and from the last strip to the waveguide exit, the scattered field is attenuated

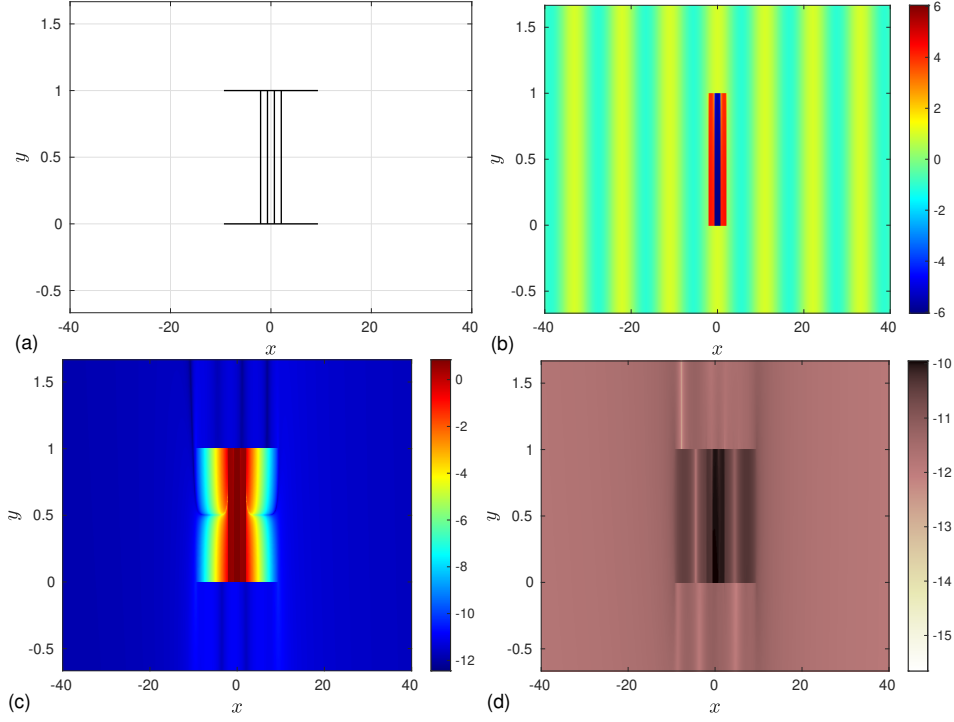


Figure 3: (a) geometry of the four-strip waveguide; (b) real part of $u(r)$; (c) \log_{10} of $|u^{\text{sc}}(r)|$; (d) \log_{10} of estimated absolute pointwise error in $u^{\text{sc}}(r)$.

due to evanescent modes. The \log_{10} of estimated absolute pointwise error in the scattered field is shown in Figure 3(d). A comparison with Figure 3(c) reveals that the amplitude of $u^{\text{sc}}(r)$ is down to the numerical noise level outside the waveguide.

As for computational performance we quote the following: with the given values of a , b , d , h , and k , the setup in Figure 3 uses 5,344 discretization points on Γ and 83 iterations in GMRES to meet a stopping criterion threshold of 10^{-14} in the estimated relative residual for the main linear system. The total execution time, including field evaluation at the 10^6 field points, is around 25 seconds.

4.1.2 B-L waveguide with four strips at doubled wavenumber

From (16) and (17) one might get the impression that if a B-L waveguide is invisible at k , then it is also invisible at wave numbers close to Nk for integers $N > 0$. This is not true since (16) and (17) are necessary but not sufficient conditions for invisibility. When k from Section 4.1.1 is doubled while b , d , and h are kept the same, then $\sigma^{\text{sc}} = 9.1 \cdot 10^{-1}$. Also the scattered near field becomes large, as seen in Figure 4.

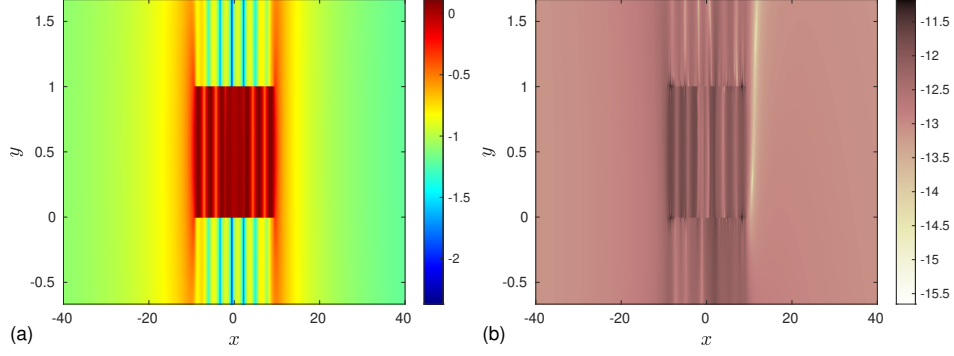


Figure 4: The four-strip waveguide at doubled wavenumber: (a) \log_{10} of $|u^{\text{sc}}(r)|$; (b) \log_{10} of estimated absolute pointwise error in $u^{\text{sc}}(r)$.

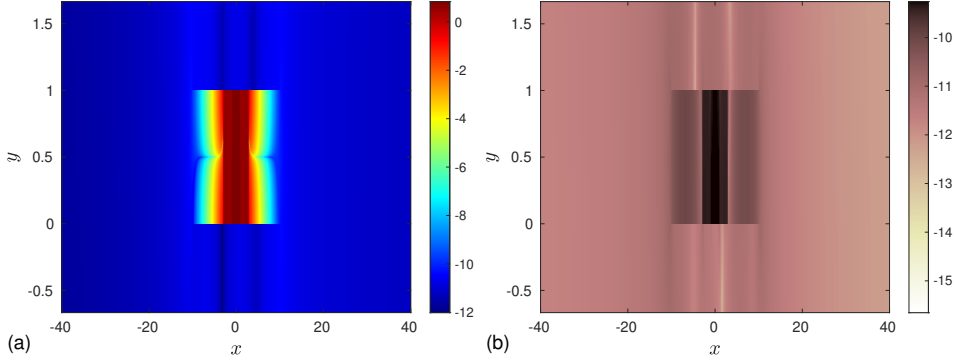


Figure 5: The four-strip waveguide with $h = 0.9997$: (a) \log_{10} of $|u^{\text{sc}}(r)|$; (b) \log_{10} of estimated absolute pointwise error in $u^{\text{sc}}(r)$.

4.1.3 Influence of length of waveguide

The B-L waveguides must have b large enough for the evanescent TM-modes to become negligible at the entrance and at the exit. In Figure 3(a) the sufficient value $b = 7.3$ is used. Smaller values of b affect the minimum value of σ^{sc} that can be reached: $b = 5$ gives $\sigma^{\text{sc}} = 2.4 \cdot 10^{-15}$ and $b = 4.3$ gives $\sigma^{\text{sc}} = 1.6 \cdot 10^{-13}$.

4.1.4 B-L waveguide with four strips and smaller gaps

The gap $a - h$, between the upper wall and the endpoints of the strips, can be both smaller and larger than in Figure 3(a) and our numerical scheme can accurately handle a wide range of gap sizes thanks to the multi-level nature of the RCIP method. Figure 5 shows $|u^{\text{sc}}(r)|$ and estimated error in $u^{\text{sc}}(r)$ for the four-strip waveguide with h increased to $h = 0.9997$. We here obtain $\sigma^{\text{sc}} = 2 \cdot 10^{-20}$ at $b = 7.3$, $k = 0.4094240286992$, and $d = 1.918010486711$.

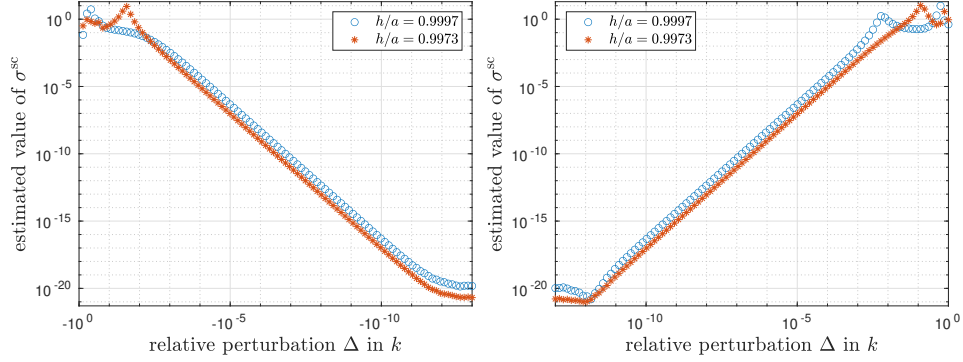


Figure 6: σ^{sc} as a function of Δ for wavenumber $k(1 + \Delta)$. Red asterisks refer to the waveguide in Figure 3 with $h = 0.9973$ and $k = 0.5712887729818$. Blue circles refer to the waveguide in Figure 5 with $h = 0.9997$ and $k = 0.4094240286992$.

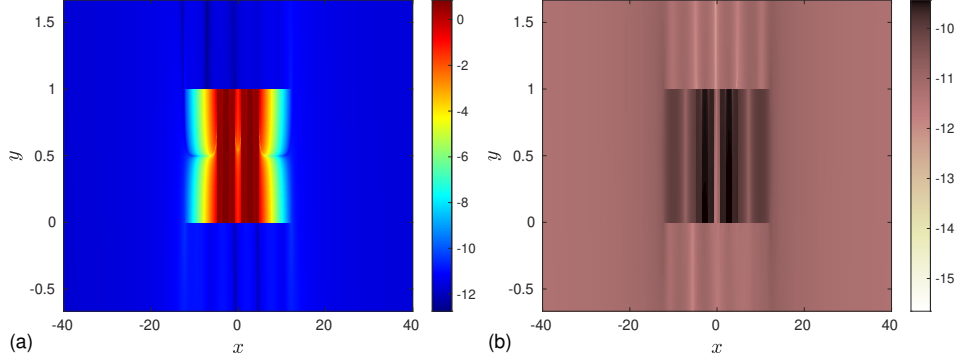


Figure 7: The eight-strip waveguide: (a) \log_{10} of $|u^{\text{sc}}(r)|$; (b) \log_{10} of estimated absolute pointwise error in $u^{\text{sc}}(r)$.

4.1.5 Bandwidth of four-strip waveguides

The width of the frequency band where a B-L waveguide is invisible can be adjusted, within certain limits, by changing h . This is illustrated in Figure 6, where the bandwidths of the waveguides in Figure 3 and Figure 5 are compared. The invisibility frequency bandwidth is tested by keeping b , d , and h , changing k to $k(1 + \Delta)$ and evaluating σ^{sc} in the interval $-1 < \Delta \leq 1$. Figure 6 shows that the relative bandwidth estimated at $\sigma^{\text{sc}} = 10^{-10}$ is 2.20 times larger for $h = 0.9973$ than for $h = 0.9997$, indicating that for a given number of strips, the relative bandwidth decreases with increasing h . We also remark that as $h \rightarrow a$, because of the corresponding smaller bandwidth, it will be progressively more difficult to find a good initial guess for k and d in the optimization procedure.

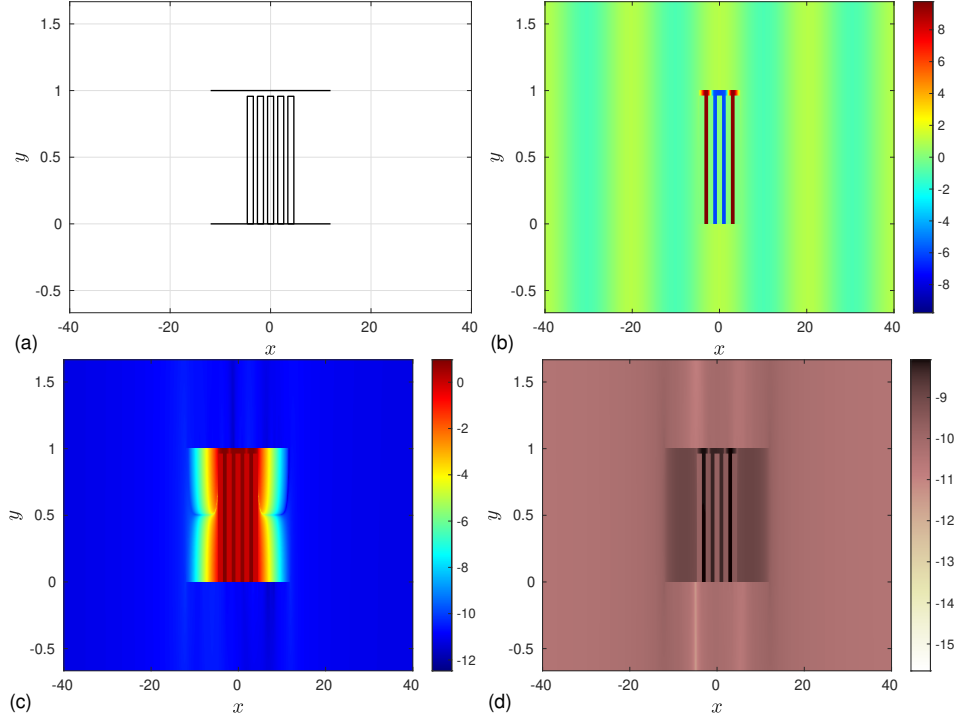


Figure 8: (a) geometry of the five-bar waveguide; (b) real part of $u(r)$; (c) \log_{10} of $|u^{\text{sc}}(r)|$; (d) \log_{10} of estimated absolute pointwise error in $u^{\text{sc}}(r)$.

4.1.6 B-L waveguide with eight strips

The eight-strip waveguide in Figure 7 has $b = 7.3$ and $h = 0.9973$, just like the four-strip waveguide in Figure 3. Optimization gives $\sigma^{\text{sc}} = 8 \cdot 10^{-21}$ at $k = 0.5710229705548$ and $d = 1.374587853864$. Thus k and d are almost the same as for the four-strip waveguide. From (16), (17), and the field $|u^{\text{sc}}(r)|$ in Figure 7(a) it follows that $u(r)$ of the eight-strip waveguide has $n = 2$ and $m = 2$. This confirms that when the number of strips is doubled then n and m are doubled while k and k_s are essentially unchanged.

4.2 B-L waveguide with rectangular barriers

The B-L waveguide in Figure 1(b) has five rectangular bars and geometric parameters $a = 1$, $b = 7.3$, $h = 0.957$, and $w = 1.2$. Optimization gives $\sigma^{\text{sc}} \approx 4 \cdot 10^{-19}$ at $k = 0.3111846733919$ and $d = 2.018021674709$. The corresponding fields and error estimates are shown in Figure 8.

Figure 8(b) shows the evaluated real part of $u(r)$. Inside the bars, where $u(r)$ should be zero, this field is everywhere less than 10^{-11} in modulus, which is satisfactory. Just like the four-strip waveguides in Figures 3 and 5, the five-bar waveguide is seen to have wavenumbers k and k_s that sat-

isfy (16) and (17) with $n = 1$ and $m = 1$. The errors in Figure 8(d) are somewhat larger than in Figures 3(d), 5(b), and 7(b), which may indicate that our numerical scheme is slightly better at handling boundaries with many endpoints than boundaries with many corners and branch points.

A bandwidth test, analogous to the one presented in Figure 6, was also made for the waveguide in Figure 8. The resulting graph of σ^{sc} as a function of Δ is almost indistinguishable from the red graph in Figure 6 and therefore not shown.

4.2.1 Resonances of inner regions

The B-L waveguide in Figure 1(b) has a Γ with five closed boundary parts and it is appropriate here to comment on a problem associated with such closed parts. The accuracy of numerical solutions to BIEs modeling exterior problems may degrade for wavenumbers close to those of inner resonances, as described in [9]. However, the lowest resonance wavenumber for the rectangles in Figure 8(a) is $\pi/w \approx 2.62$, which, compared to $k = 0.3111846733919$, is far too large to cause any problems. Therefore, the problem of inner resonances is not an issue in this work.

4.3 Optimization in two steps

To speed up the optimization, we first optimized the B-L waveguides and corresponding wavenumbers using simplified geometries and the Acoustic module in the FEM software package COMSOL Multiphysics version 6.1. A simplified geometry is bounded and consists of a B-L waveguide with an input port at the left end and an output port at the right end. A TEM mode is launched at the input port. Based on given values of geometric parameters, a wavenumber is identified for which the reflected field at the input port is close to zero. By adjusting the geometry, this wavenumber is shifted until the criterion in (16) is satisfied for $n = 1$. The geometry and the wavenumber are then further adjusted so that the reflected field and the difference between the transmitted and incident fields are minimized. The adjusted geometry and wavenumber so obtained then serve as the initial guess for optimization using our BIE technique. As an example, the initial guess for the waveguide in Figure 3 is produced using the finest predefined mesh in COMSOL, with 120,000 degrees of freedom, and gives an initial-guess scattering cross section of $\sigma^{\text{sc}} \approx 7 \cdot 10^{-4}$.

4.4 Additional comments to the examples

Our examples show that B-L waveguides can be rendered invisible for an incident in-plane TM wave. In a narrow frequency band, the scattered field is then close to zero everywhere outside the waveguide. This means that several B-L waveguides can be combined to form a larger invisible structure. Such a

structure may be an alternative to an FSS in applications that involve band pass structures. For the B-L waveguide with rectangular bars, it is possible to hide other objects inside the bars. This is then a perfect cloaking for a TM wave at normal incidence and, for that wave, it is a much better cloaking than that achieved by today’s metamaterials. On the other hand, cloaking with metamaterials has the advantage of being independent of the polarization and angle of incidence of the incident plane wave.

The height h of the barriers is close to a (small gap) in all examples. We have not tested for what values of h invisible B-L waveguides exist, but this is certainly an interesting issue.

Another thing that should be interesting to investigate is the effect of PEC-barrier shape on invisibility. That is, barriers of other shapes than strips and bars. Even dielectric barriers might be an option. Regardless of the type of barriers, it is crucial that the barriers form a finite periodic array.

5 Conclusions

We have shown that B-L waveguides can be designed to become invisible in a frequency band of prescribed center frequency and, within certain limits, width. The specific examples presented have barriers with endpoints, corners, and branch points. We seek to design waveguides with scattering cross sections on the order of 10^{-18} . This requires a robust numerical scheme that can accurately resolve the Neumann Helmholtz problem close to singular boundary points. Such a scheme has been developed by us and is reviewed and used in this work.

References

- [1] D. Agarwal, M. O’Neil, and M. Rachh. FMM-accelerated solvers for the Laplace-Beltrami problem on complex surfaces in three dimensions. *J. Sci. Comput.*, 97(1):Paper No. 25, 25 pp., 2023.
- [2] E. Andersson. Implementation and study of boundary integral operators related to PDE:s in the plane. Master’s Theses in Mathematical Sciences 2023:E27, Centre for Mathematical Sciences, Lund University, 2023. <https://lup.lub.lu.se/student-papers/record/9133621>.
- [3] R. S. Anwar, L. Mao, and H. Ning. Frequency selective surfaces: A review. *Appl. Sci.*, 8(9): Paper No. 1689, 46 pp., 2018.
- [4] G. B. Arfken and H. J. Weber. *Mathematical methods for physicists*. Elsevier, Amsterdam, sixth edition, 2005.
- [5] A.-S. Bonnet-Ben Dhia, E. Lunéville, Y. Mbeutcha, and S. Nazarov. A method to build non-scattering perturbations of two-dimensional acoustic waveguides. *Math. Meth. Appl. Sci.*, 40(2):335–349, 2017.

- [6] V. E. Boria and B. Gimeno. Waveguide filters for satellites. *IEEE Microw. Mag.*, 8(5):60–70, 2007.
- [7] O. P. Bruno and S. K. Lintner. Second-kind integral solvers for TE and TM problems of diffraction by open arcs. *Radio Sci.*, 47(6): Paper No. RS6006, 13 pp., 2012.
- [8] L. Chesnel, J. Heleine, and S. A. Nazarov. Acoustic passive cloaking using thin outer resonators. *Z. Angew. Math. Phys.*, 73(3): Paper No. 98, 31 pp., 2022.
- [9] W. Chew and J. Song. Gedanken experiments to understand the internal resonance problems of electromagnetic scattering. *Electromagn.*, 27(8):457–471, 2007.
- [10] D. Colton and R. Kress. *Inverse acoustic and electromagnetic scattering theory*, volume 93 of *Applied Mathematical Sciences*. Springer-Verlag, Berlin, second edition, 1998.
- [11] J. Fan, L. Zhang, S. Wei, Z. Zhang, S.-K. Choi, B. Song, and Y. Shi. A review of additive manufacturing of metamaterials and developing trends. *Mater. Today*, 50:303–328, 2021.
- [12] G. Gbur. Invisibility physics: past, present, and future. In *Progress in Optics*, volume 58, pages 65–114. Elsevier, 2013.
- [13] Z. Gimbutas, L. Greengard, M. O’Neil, M. Rachh, and V. Rokhlin. *fmm2d software library*. <https://github.com/flatironinstitute/fmm2d>. Accessed: 2023-04-17.
- [14] S. Hao, A. H. Barnett, P. G. Martinsson, and P. Young. High-order accurate methods for Nyström discretization of integral equations on smooth curves in the plane. *Adv. Comput. Math.*, 40(1):245–272, 2014.
- [15] J. Helsing. Solving integral equations on piecewise smooth boundaries using the RCIP method: a tutorial. *arXiv e-prints*, arXiv:1207.6737v10 [physics.comp-ph], revised 2022.
- [16] J. Helsing and S. Jiang. Solving Dirichlet and Neumann Helmholtz problems on piecewise smooth open curves. 2023. In preparation.
- [17] J. Helsing and A. Karlsson. An accurate boundary value problem solver applied to scattering from cylinders with corners. *IEEE Trans. Antennas Propag.*, 61(7):3693–3700, 2013.
- [18] J. Helsing and A. Karlsson. On a Helmholtz transmission problem in planar domains with corners. *J. Comput. Phys.*, 371:315–332, 2018.
- [19] J. Helsing and R. Ojala. Elastostatic computations on aggregates of grains with sharp interfaces, corners, and triple-junctions. *Internat. J. Solids Structures*, 46(25):4437–4450, 2009.
- [20] M. Kadic, G. W. Milton, M. van Hecke, and M. Wegener. 3D metamaterials. *Nat. Rev. Phys.*, 1(3):198–210, 2019.
- [21] S. P. Shipman and H. Tu. Total resonant transmission and reflection by periodic structures. *SIAM J. Appl. Math.*, 72(1):216–239, 2012.